# Fast identification of mineral inclusions in diamond at GSECARS using synchrotron X-ray microtomography, radiography, and diffraction

Michelle D. Wenz,<sup>1</sup> Steven D. Jacobsen,<sup>1</sup> Dongzhou Zhang<sup>2</sup>, Margo Regier<sup>5</sup>, Hannah J. Bausch<sup>1</sup>, Przemyslaw K. Dera<sup>2</sup>, Mark Rivers<sup>3</sup>, Peter Eng<sup>3</sup>, Steven B. Shirey<sup>4</sup>, and D. Graham Pearson<sup>5</sup>

<sup>1</sup>Department of Earth and Planetary Science, Northwestern University, Evanston, Illinois 60208, USA <sup>2</sup>Hawaii Institute of Geophysics and Planetology, University of Hawaii, Honolulu, Hawaii 96822, USA <sup>3</sup>Center for Advanced Radiation Sources, The University of Chicago, Chicago, Illinois 60637, USA

<sup>4</sup>Department of Terrestrial Magnetism, Carnegie Institution for Science, Washington DC 20015, USA <sup>5</sup>Department of Earth and Atmospheric Sciences, University of Alberta, Edmonton, Alberta T6G 2E9,

Canada

- 13 Keywords: diamond, minerals, microinclusions, computed microtomography, microdiffraction, 14 radiography, high-throughput
- 15 Synopsis: Microinclusions in diamond reveal geochemical signatures from the Earth's deep mantle.
- 16 A methodology is developed for non-destructive, high-throughput in-situ characterization of
- 17 mineral inclusions using synchrotron X-ray microtomgraphy, radiography and diffraction at
- 18 GSECARS, Sector 13 of the Advanced Photon Source.
- 19 Abstract
  - Mineral inclusions in natural diamond are widely studied for the insight that they provide into the geochemistry and dynamics of the Earth's interior. A major challenge in achieving thorough, yet high rates of analysis of mineral inclusions in diamond derives from the micrometer-scale of most inclusions, often requiring synchrotron radiation sources for diffraction. Centering microinclusions for diffraction with a highly-focused synchrotron beam cannot be achieved optically because of the very high index of refraction of diamond. We developed a fast, high-throughput method for identification of micromineral inclusions in diamond at GeoSoilEnviro Center for Advanced Radiation Sources (GSECARS), Advanced Photon Source (APS), Argonne National Laboratory (ANL). Diamonds and their inclusions are imaged using synchrotron 3D computed X-ray microtomography on beamline 13-BM-D of GSECARS. The location of every inclusion is then pinpointed onto the coordinate system of the 6-circle goniometer of the single-crystal diffractometer on beamline 13-BM-C. Because the bending magnet branch 13-BM is divided and delivered into 13-BM-C and 13-BM-D stations simultaneously, numerous diamonds

can be examined during coordinated runs. The fast, high-throughput capability of the methodology is demonstrated by collecting 3D diffraction data on 51 diamond inclusions from Juína, Brazil, within about 72 total hours of beamtime.

### 1. Introduction

33

34

35

36

37

38

39

40

41

42

43

44

45

46

47

48

49

50

51

52

53

54

55

56

Most diamonds are thought to crystalize in the mantle roots of the continental lithosphere (Stachel & Harris 2008), whereas so-called super-deep diamonds and their inclusions are believed to crystalize in the convecting upper mantle, transition zone, and even lower mantle (Nestola et al., 2018; Palot et al., 2016; Pearson et al., 2014; Pearson et al., 2003; Shirey et al., 2013; Stachel et al., 2005). Provided that the host diamonds are not cracked, minerals included within them are essentially encapsulated in an inert preservation vessel during eruption to the surface in kimberlitic magmas. The study of these micromineral inclusions provides insight into the geochemistry and dynamics of the Earth's crust-mantle system from otherwise unattainable depths (Harte, 2011; Pearson et al., 2014; Smith et al., 2018). In the past, the study of diamond inclusions has been largely limited to destructive techniques, such as breaking the diamond to release inclusions or grinding away the host diamond to expose inclusions at the surface. In addition, the use of laboratory-source X-rays limits the minimum size of inclusion that can be identified by X-ray diffraction. Destructive extraction techniques have the inherent risk of losing or altering the inclusions, which are usually under remnant pressure inside the diamond host (Angel et al., 2015). Thus, by studying these encapsulated inclusions using non-destructive methods, properties like inclusion pressure, oxidation state, high-pressure phases, and volatile content remain preserved.

To date, in-situ identification of mineral inclusions in diamond via non-destructive methods remains challenging as the very-high refractive index of diamond ( $n \sim 2.4$ ) hinders typical identification methods, such as optical microscopy or Raman spectroscopy, unless the

inclusion is very close to a flat diamond surface. The high n of diamond also makes optical centering methods for single-crystal diffraction time consuming (Kunz et al., 2002; Nestola et al., 2012). In 2011, the first in-situ crystal structure refinement of an inclusion in diamond was performed on an olivine crystal measuring ~80  $\mu$ m in largest dimension using a sealed-tube Mo  $K\alpha$  source (Nestola et al., 2011). In that study, two large and parallel faces of the diamond facilitated optical centering of the inclusion. Subsequently, synchrotron radiation has been employed to carry out in-situ structure refinements of clinopyroxenes entrapped in diamond (Nestola et al., 2016). Centering microinclusions inside highly irregular diamonds with an X-ray beam for diffraction can be accomplished by combining tomography with X-ray diffraction. Recently, this combined approach was employed by Nestola et al. (2012) using lab sources in Padova, Italy. The use of a lab source is ideal for the study of large (>50  $\mu$ m) inclusions, but a method to quickly identify the multitude of smaller inclusions in large, available suites of superdeep diamonds is required to obtain a more thorough sampling of inclusion mineralogy.

In this paper we describe a fast, high-throughput and non-destructive methodology for identifying microinclusions in diamond as small as 10-20 µm in maximum dimension by combining synchrotron microtomography with a newly-developed radiography system now installed on the single-crystal diffraction beamline of GSECARS, Advanced Photon Source. Such a fast yet thorough method allows for all inclusions within the full volume of each diamond to be identified, thus allowing for a better relative modal proportion of inclusions to be obtained as smaller inclusions, which would be missed in optical methods are not overlooked. In addition, the use of microtomography prior to diffraction provides detailed information on the integrity of the diamond host, revealing microcracks that may indicate the potential for metasomatic alteration of the inclusions. By identifying all microinclusions within a suite of super-deep

diamonds more information about the environment wherein superdeep diamonds form is obtained. The efficiency of the system is demonstrated by collecting 3D diffraction data from fifty inclusions in 23 total different diamonds from Juína, Brazil, all within a total of about 72 hours of beamtime. This result is unachievable by any other method.

# 2. Experimental

80

81

82

83

84

85

86

87

88

89

90

91

92

93

94

95

96

97

98

99

100

101

102

# 2.1. Synchrotron Microtomography

Synchrotron microtomography was used to physically locate mineral inclusions within the diamond was conducted at GSECARS, beamline 13-BM-D of the APS. The configuration of the 13-BM branch allows for simultaneous delivery of the X-ray beam to both 13-BM-D (microtomography) and 13-BM-C (single-crystal X-ray diffraction) beamlines. Thus, during coordinated runs the diamonds go directly from 13-BM-D to the newly developed 2D radiography and single-crystal diffraction system at 13-BM-C, which hosts the Partnership for eXtreme Xtallography (PX<sup>2</sup>) facility, a collaboration between University of Hawaii and GSECARS supported by the Consortium for Materials Properties Research in the Earth Science (COMPRES). This facility is funded by COMPRES to advance crystallographic studies of minerals and materials at condition of extreme pressures, temperatures and strain rates. A schematic diagram of the microtomography beamline illustrates the configuration used for superdeep diamonds many of which have irregular shapes (Fig. 1). A monochromatic beam with an energy of 28.9 keV was chosen for this approach as this energy closely matches the operating energy of the 13-BM-C (28.6 keV) diffraction beamline. Due to the diffraction of the scintillator itself, Ce-doped LuAG, the exact operation energy of 13-BM-C could not be used as artifacts appeared in the tomographic reconstructions. Choosing a similar operating energy guarantees that all inclusions visible at 13-BM-D beamline will also appear in the 2D radiography system at

13-BM-C. Due to the variability in both size and shape of super-deep diamonds, an adjustable field of view is required to accurately map all inclusions. A typical field of view for large diamonds (~6 mm) is around 8.70 mm by 5.44 mm. Collection times are on the order of fifteen minutes per diamond, thus within a 24-hour time period full tomography on the entire volume of over 90 diamonds is achievable.

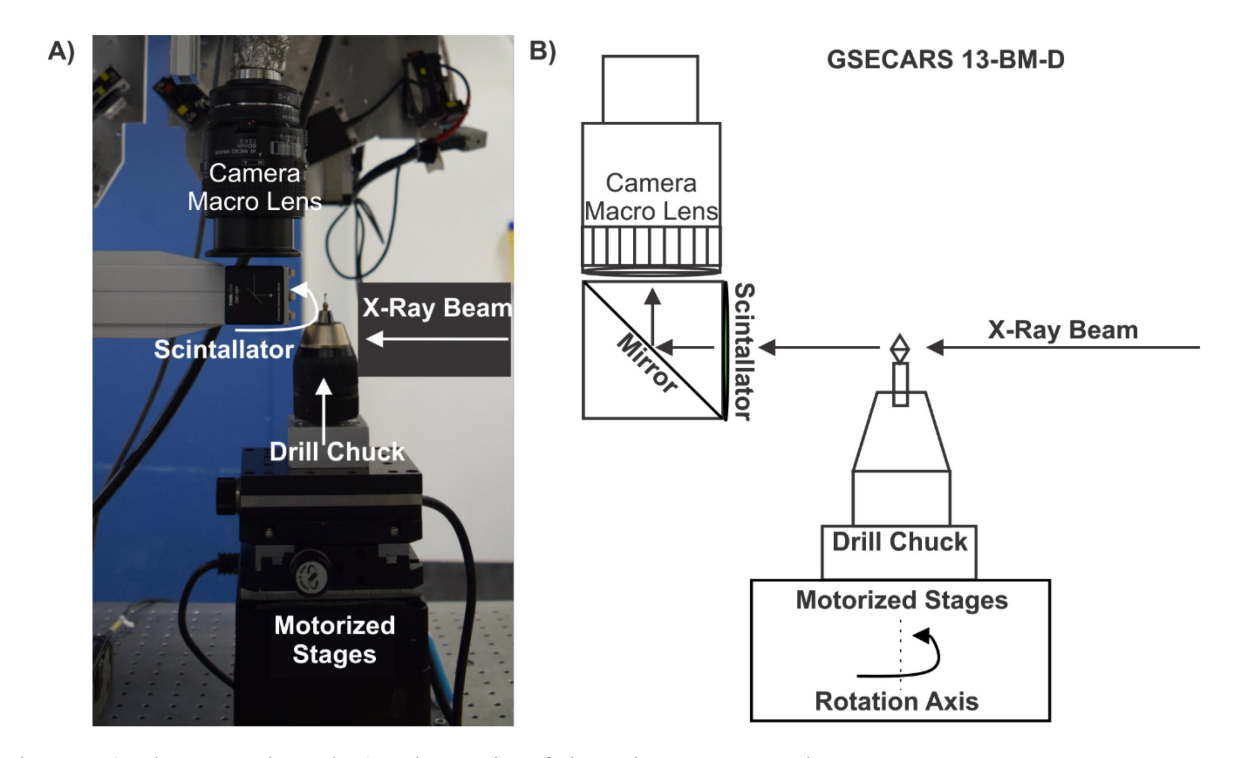


Fig. 1. A) Photograph and B) schematic of the microtomography setup at 13-BM-D, GSECARS, Advanced Photon Source.

# 2.2. Synchrotron X-ray Diffraction

Single-crystal X-ray diffraction measurements were carried out at GSECARS, beamline 13-BM-C of the APS. Combining microtomography and X-ray diffraction required development of a portable 2D radiography attachment at 13-BM-C for the centering procedure. The components of this live radiograph system consist of a scintillator, mirror, a 5x objective, and a GigE camera. All components are mounted to a motorized stage, which enables the radiography

system to drive in and out of the X-ray beam. Thus, the 2D radiography setup does not interfere with the 6-circle goniometer during the diffraction collection. EPICS areaDetector (Rivers, 2018; Rivers, 2010) and ImageJ (Schneider et al., 2012) is used to view the live radiograph while allowing for the constant normalization to a flat field image.

The first step to setup the diffraction experiment is to identify the rotation axis of the diffractometer and intersect the X-ray beam with it. The rotation axis of the diffractometer is setup in the horizontal direction that is perpendicular to the incident X-ray (Zhang et al., 2017). A focused X-ray beam with a full width at the half maximum of 12 µm (H) by 18 µm (V) is achieved by horizontal and vertical Kirkpatrick-Baez mirrors (Eng et al., 1998). The rotation axis of the diffractometer is visualized by rotating a 25 µm diameter tungsten wire. Once the tungsten wire ceases to precess during rotation, the tungsten wire coincides with the rotation axis. The X-ray beam vertical position is then adjusted until maximum absorption is detected. At this stage, the X-ray beam intersects the rotation axis of the diffractometer and the tungsten wire is then removed. The incident beam position is marked on the scintillator's image with a virtual crosshair, which corresponds to the intersection of the rotation axis and the X-ray.

Obtaining a live radiograph image of the inclusion on the 13-BM-C diffraction beamline requires defocusing the X-ray beam to increase the field of view (FOV). An FOV of ~100 µm (H) by 250 µm (V) is achieved by defocusing the Kirkpatrick-Baez mirrors, giving a magnified image of the inclusion for centering (Fig. 2). Each inclusion is located by observing its characteristic absorption shadow in the radiograph image. Locating inclusions in this magnified FOV requires the use of the high-resolution (4.5 mm/pixel) microtomography data obtained at beamline 13-BM-D prior to diffraction. Without microtomography data it can take an hour or more to locate an inclusion within such a magnified FOV, whereas with the microtomography

map it takes only a few minutes. Once an inclusion is found within the FOV and placed into the virtual crosshair, a rotation-centering of the inclusion is performed at 5-degree steps thus centering the inclusion on the rotation axis. Once the inclusion is properly centered, the X-ray beam then is refocused back to the virtual crosshair, and the scintillator is driven out of the beam path. Single-crystal X-ray diffraction using the 6-circle goniometer proceeds following standard X-ray diffraction protocols (Zhang et al., 2017). It takes 5 minutes to collect a wide-scan diffraction image (rotation of 180°) and 30 minutes for step scan collections (steps in scan 180, exposure time per degree 1 sec, rotation of 180°) using the MAR 165 CCD detector. The new Pilatus 1M detector with a 1 mm silicon sensor implemented in 2019 will speed these collections times up to a few minutes. Thus, 13-BM-C allows for fast diffraction imaging on a multitude of inclusions.

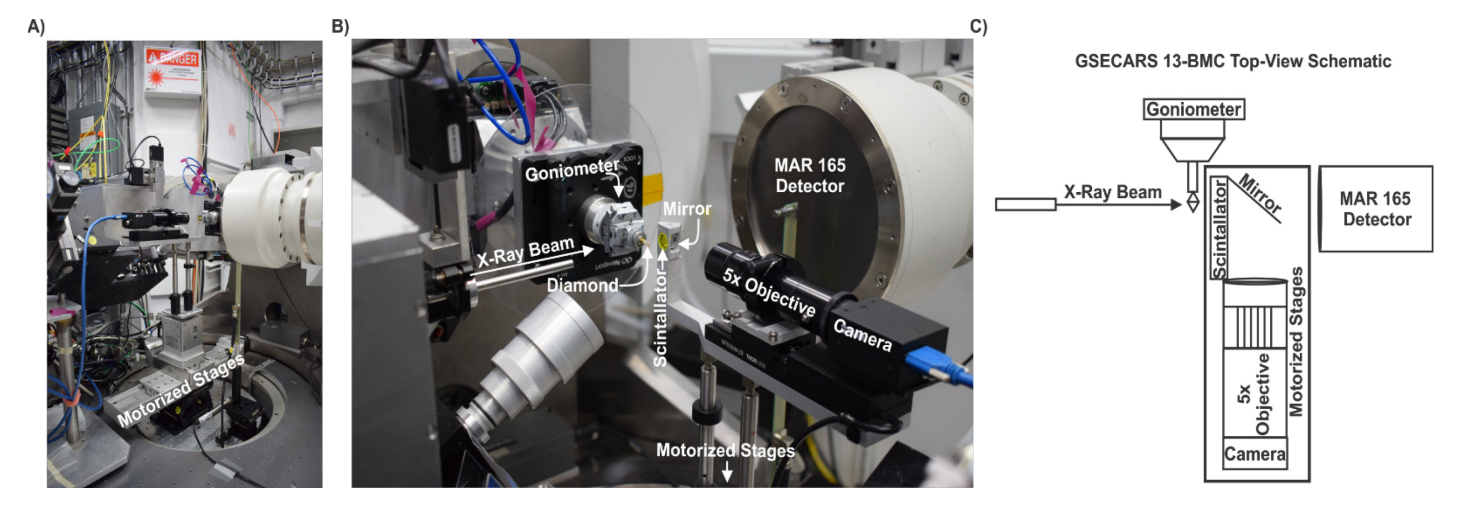


Fig. 2. A) Photograph of the entire portable radiograph attachment. B) Close up photograph of the portable radiograph system. C) A top-view schematic of the portable radiograph system at 13-BM-C. The rectangle represents the motorized stage, yet also highlights the main components that make up the newly developed portable 2D radiograph system available at 13-BM-C.

#### 3. Results

To demonstrate the capabilities of this new fast, high-throughput combined synchrotron microtomography and X-ray diffraction technique, a suite of sixty-one diamonds from Juína, Brazil were studied. Microtomography data were collected on all sixty-one diamonds using a

CMOS camera with 1920x1200 pixels, 4.5 micron pixel size on the sample, 1 second exposure time, and 900 projections. All microtomography data on the sixty-one diamonds were collected within a 24-hour period.

162

163

164

165

166

167

168

169

170

171

172

173

174

175

176

177

178

179

180

181

182

183

184

X-ray diffraction data, obtained using the newly developed live 2D radiograph centering technique at 13-BM-C, were collected on fifty-one inclusions found within twenty-three of these super-deep diamonds within a 72-hour period. Sample to detector distances and tilt were calibrated using diffraction of LaB<sub>6</sub>. Single-crystal inclusion diffraction data were processed using the ATREX (previously GSE ADA) (Dera et al., 2013) program, which handles peak searching and fitting routines allowing for the generation of a peak list. To index the peaks, the peak list generated in ATREX is read into the Reciprocal Space Viewer (RSV) (Dera et al., 2013) program, where peak indexing, orientation matrix determination and refinement of lattice parameters is performed. For powder inclusions as well as mixed phase inclusions (inclusions with both powder and single-crystal phases) diffraction images were first integrated in DIOPTAS (Prescher & Prakapenka, 2015), a program designed specifically for handling the large amounts of data collected at XRD beamlines, to generate intensity versus  $2\theta$  plots. These  $2\theta$  plots were then imported into the General Structure and Analysis System II (GSAS-II) (Toby &Von Dreele, 2013) program, for further processing, indexing, and refinement of lattice parameters. Inclusions were ultimately identified via their lattice parameters.

Lattice parameters for the fifty-one inclusions are shown in Table I. A summary of all minerals found from these diamonds is given in Table II. The majority of inclusion phases form solid solutions. Thus, unit-cell volumes are dependent on both composition and remnant pressure. Phases along the hematite (Fe<sub>2</sub>O<sub>3</sub>) to ilmenite (FeTiO<sub>3</sub>) solid solution are referred to as titanohematite (Brown et al., 1993). Phases along the magnetite (Fe<sub>3</sub>O<sub>4</sub>) to ulvöspinel (Fe<sub>2</sub>TiO<sub>4</sub>)

solid solution are referred to as titanomagnetite (Bosi et al., 2009). Olivine phases refer to those along the forsterite (Mg<sub>2</sub>SiO<sub>4</sub>) to fayalite (Fe<sub>2</sub>SiO<sub>4</sub>) solid solution series. Following standard mineralogical nomenclature the (Mg,Fe)O oxides are classified such that samples containing <50 mol% FeO are referred to as ferropericlase and those with >50 mol% are magnesiowüstite (Jacobsen et al. 2002; Prewitt and Downs, 1998). We note however that there is large uncertainty in the composition of such inclusions studied in situ with lattice parameters alone. For (Mg,Fe)O, assuming the variation of lattice parameter with  $X_{Fe} = \Sigma Fe/(\Sigma Fe+Mg)$  and an average bulk modulus  $K_{T0}$  of 160 GPa from the study of Jacobsen et al. (2002), the value of  $X_{Fe}$  would be underestimated by about 0.088 (or 8.8 mol% FeO) per GPa of remnant pressure.

It is interesting to note that the majority of the inclusions identified in our study are ferropericlase (Mg,Fe)O. Ferropericlase is reported previously as a predominate mineral in Juína diamonds, and it often has been associated with signifying a lower mantle origin (Anzolini et al., 2019; Kaminsky, et al., 2009), whereas more non-pyrolitic, Fe-rich (Mg,Fe)O inclusions are associated with conditions of diamond growth (Nimis et al. 2018). Thomson et al. (2016) proposed that the presence of (Mg,Fe)O inclusions may be related to the reactions between the carbonatitic melt and reduced mantle peridotite. The range of intermediate and Fe-rich compositions reported in ferropericlase inclusions in diamond may represent different stages of the reaction (Thomson et al., 2016). Because the numerous ferropericlase inclusions in the current suite of Juína diamonds are not associated with any high-pressure mineral inclusions, they are possibly associated with the melt reactions proposed by Thomson et al. (2016) and Nimis et al. (2018).

Table 1: Symmetry-constrained lattice parameters of fifty-one inclusions identified in a suite of diamonds from São Luiz locality in Juína, Brazil. Single crystal inclusions denoted by \* superscript the rest of the inclusions are powder.

Inclusion	a (Å)	<b>b</b> (Å)	c (Å)	α (°)	β (°)	γ (°)	Volume (ų)	Symmetry Constraints	Mineral
6b_04b*	8.509(2)	8.509(2)	8.509(2)	90	90	90	616.0(2)	cubic	titanomagnetite Fe <sub>1+x</sub> (Fe <sub>2-2x</sub> Ti <sub>x</sub> )O <sub>4</sub>
	4.255(1)	4.255(1)	4.255(1)	90	90	90	77.1(6)	cubic	ferropericlase (Mgx,Fe <sub>1-x</sub> )O
6b_05a*	4.246(4)	4.246(4)	4.246(4)	90	90	90	76.6(2)	cubic	ferropericlase (Mgx,Fe <sub>1-x</sub> )O
6b_05b*	4.255(2)	4.255(2)	4.255(2)	90	90	90	77.0(2)	cubic	ferropericlase (Mgx,Fe <sub>1-x</sub> )O
6b_05c*	4.259(1)	4.259(1)	4.259(1)	90	90	90	77.3(1)	cubic	magnesiowüstite (Mg <sub>1-x</sub> ,Fe <sub>x</sub> )O
6b_05d*	4.262(2)	4.262(2)	4.262(2)	90	90	90	77.4(2)	cubic	magnesiowüstite (Mg <sub>1-x</sub> ,Fe <sub>x</sub> )O
6b_05e*	4.251(2)	4.251(2)	4.251(2)	90	90	90	77.4(2)	cubic	ferropericlase (Mgx,Fe <sub>1-x</sub> )O
6b_06a*	4.276(2)	4.276(2)	4.276	90	90	90	78.2(1)	cubic	magnesiowüstite (Mg <sub>1-x</sub> ,Fe <sub>x</sub> )O
6b_06b*	4.271(7)	4.271(7)	4.271(7)	90	90	90	77.9(1)	cubic	magnesiowüstite (Mg <sub>1-x</sub> ,Fe <sub>x</sub> )O
6b_07a	2.868(9)	2.868(9)	2.868(9)	90	90	90	23.6(2)	cubic	Fe (bcc) with some alloy
6b_07b	2.868(5)	2.868(5)	2.868(5)	90	90	90	23.6(1)	cubic	Fe (bcc) with some alloy
6b_07c*	4.276(2)	4.276(2)	4.276(2)	90	90	90	78.2(1)	cubic	magnesiowüstite (Mg <sub>1-x</sub> ,Fe <sub>x</sub> )O
6b_07c2*	8.442(5)	8.442(5)	8.442(5)	90	90	90	601.7(3)	cubic	titanomagnetite $Fe_{1+x}(Fe_{2-2x}Ti_x)O_4$
6b_07d*	4.204(5)	4.204(5)	4.204(5)	90	90	90	75.3(3)	cubic	ferropericlase (Mgx,Fe <sub>1-x</sub> )O
6b_07d2*	8.511(1)	8.511(1)	8.5107	90	90	90	601.7(3)	cubic	titanomagnetite Fe <sub>1+x</sub> (Fe <sub>2-2x</sub> Ti <sub>x</sub> )O <sub>4</sub>
6b_07e*	4.320(7)	4.320(7)	4.320(7)	90	90	90	81.0(4)	cubic	wüstite FeO
6b_07e2*	8.490(5)	8.490(5)	8.490(5)	90	90	90	612.0(2)	cubic	titanomagnetite Fe <sub>1+x</sub> (Fe <sub>2-2x</sub> Ti <sub>x</sub> )O <sub>4</sub>
6b_08c*	5.083(1)	5.083(1)	5.083(1)	90	90	120	314.6(3)	hexagonal	ilmenite FeTiO <sub>3</sub>
6b 09	4.640(6)	10.005(9)	3.028(3)	90	90	90	140.6(2)	orthorhombic	goethite (FeOOH)
6b 10b	5.032(1)	5.032(1)	13.759(3)	90	90	120	301.7(1)	hexagonal	hematite Fe <sub>2</sub> O <sub>3</sub>
6b_10c	5.140(3)	5.140(3)	13.420(2)	90	90	120	307.5(2)	hexagonal	titanohematite (xFeTiO <sub>3</sub> [1-x]Fe <sub>2</sub> O <sub>3</sub> )
6b 11b*	8.396(2)	8.396(2)	8.396(2)	90	90	90	591.8(2)	cubic	magnetite Fe <sub>3</sub> O <sub>4</sub>
6b_12a*	4.273(2)	4.273(2)	4.273(2)	90	90	90	78.0(3)	cubic	magnesiowüstite (Mg <sub>1-x</sub> ,Fe <sub>x</sub> )O
6b_12b*	4.270(1)	4.270(1)	4.270(1)	90	90	90	77.9(2)	cubic	magnesiowüstite (Mg <sub>1-x</sub> ,Fe <sub>x</sub> )O
6b_12c*	4.280(9)	4.280(9)	4.2796	90	90	90	78.4(5)	cubic	magnesiowüstite (Mg <sub>1-x</sub> ,Fe <sub>x</sub> )O

6b 12d*	4.274(3)	4.274(3)	4.274(3)	90	90	90	78.1(5)	cubic	magnesiowüstite (Mg <sub>1-x</sub> ,Fe <sub>x</sub> )O
6b_17b*	4.270(1)	4.270(1)	4.270(1)	90	90	90	77.8(2)	cubic	magnesiowüstite (Mg <sub>1-x</sub> ,Fe <sub>x</sub> )O
6b 17c*	4.285(1)	4.285(1)	4.285(1)	90	90	90	78.7(5)	cubic	magnesiowüstite (Mg <sub>1-x</sub> ,Fe <sub>x</sub> )O
6b 21c*	4.279(2)	4.279(2)	4.279(2)	90	90	90	78.3(2)	cubic	magnesiowüstite (Mg <sub>1-x</sub> ,Fe <sub>x</sub> )O
6b 21c2	8.405(2)	8.405(2)	8.405(2)	90	90	90	593.8(2)	cubic	titanomagnetite Fe <sub>1+x</sub> (Fe <sub>2-2x</sub> Ti <sub>x</sub> )O <sub>4</sub>
6b 23*	4.232(8)	4.232(8)	4.232(8)	90	90	90	75.8(3)	cubic	ferropericlase (Mg <sub>x</sub> ,Fe <sub>1-x</sub> )O
6b 29a*	4.261(2)	4.261(2)	4.261(2)	90	90	90	77.8(2)	cubic	magnesiowüstite (Mg <sub>1-x</sub> ,Fe <sub>x</sub> )O
6b_29b*	4.253(1)	4.253(1)	4.253(1)	90	90	90	76.9(1)	cubic	ferropericlase (Mgx,Fe <sub>1-x</sub> )O
6b_34a*	4.243(2)	4.243(2)	4.243(2)	90	90	90	76.4(2)	cubic	ferropericlase (Mgx,Fe <sub>1-x</sub> )O
6b_34b*	4.245(1)	4.245(1)	4.24489	90	90	90	76.5(1)	cubic	ferropericlase (Mg <sub>x</sub> ,Fe <sub>1-x</sub> )O
6b_34c*	4.252(2)	4.252(2)	4.252(2)	90	90	90	76.8(2)	cubic	ferropericlase (Mg <sub>x</sub> ,Fe <sub>1-x</sub> )O
6b_37a	4.254(2)	4.254(2)	4.254(2)	90	90	90	77.0(2)	cubic	ferropericlase (Mgx,Fe <sub>1-x</sub> )O
	8.379(2)	8.379(2)	8.379(2)	90	90	90	588.0(4)	cubic	magnetite Fe <sub>3</sub> O <sub>4</sub>
6b_39a	5.037(5)	5.037(5)	13.769(1)	90	90	120	302.5(4)	hexagonal	titanohematite (xFeTiO <sub>3</sub> [1-x]Fe <sub>2</sub> O <sub>3</sub> )
6b_39b	5.038(7)	5.038(7)	13.761(1)	90	90	120	302.5(5)	hexagonal	titanohematite (xFeTiO <sub>3</sub> [1-x]Fe <sub>2</sub> O <sub>3</sub> )
6b_46*	11.584(3)	11.584(3)	11.584(3)	90	90	90	1554.4(6)	cubic	almandine Fe <sub>3</sub> Al <sub>2</sub> (SiO <sub>4</sub> ) <sub>3</sub>
6b_48b	4.744(4)	10.185(1)	5.978(7)	90	90	90	288.8(6)	orthorhombic	olivine (Mg <sub>x</sub> ,Fe <sub>2-x</sub> ) <sub>2</sub> SiO <sub>4</sub>
6b_53*	4.246(1)	4.246(1)	4.246(1)	90	90	90	76.5(1)	cubic	ferropericlase (Mgx,Fe <sub>1-x</sub> )O
6b_54b*	6.609(2)	6.609(2)	6.001(3)	90	90	90	262.1(2)	tetragonal	zircon ZrSiO <sub>4</sub>
6b_56a	4.758(7)	10.209(6)	5.972(7)	90	90	90	290.1(4)	orthorhombic	olivine (Mg <sub>x</sub> ,Fe <sub>2-x</sub> ) <sub>2</sub> SiO <sub>4</sub>
6b_56b	4.759(8)	10.209(8)	5.976(1)	90	90	90	290.4(5)	orthorhombic	olivine (Mg <sub>x</sub> ,Fe <sub>2-x</sub> ) <sub>2</sub> SiO <sub>4</sub>
	8.394(6)	8.394(6)	8.394(6)	90	90	90	591.4(1)	cubic	magnetite Fe <sub>3</sub> O <sub>4</sub>
6b_56c	4.754(1)	10.205(7)	5.978(1)	90	90	90	290.0(6)	orthorhombic	olivine (Mg <sub>x</sub> ,Fe <sub>2-x</sub> ) <sub>2</sub> SiO <sub>4</sub>
6b_56d	4.756(1)	10.206(1)	5.981(1)	90	90	90	290.3(6)	orthorhombic	olivine (Mg <sub>x</sub> ,Fe <sub>2-x</sub> ) <sub>2</sub> SiO <sub>4</sub>
5a_09a	5.077(3)	5.077(3)	13.894(4)	90	90	120	310.1(2)	hexagonal	titanohematite (xFeTiO <sub>3</sub> [1-x]Fe <sub>2</sub> O <sub>3</sub> )
5a_09b	5.069(2)	5.069(2)	13.931(5)	90	90	120	310.1(2)	hexagonal	titanohematite (xFeTiO <sub>3</sub> [1-x]Fe <sub>2</sub> O <sub>3</sub> )
5a_10f*	4.281(8)	4.281(8)	4.281(8)	90	90	90	78.5(4)	cubic	magnesiowüstite (Mg <sub>1-x</sub> ,Fe <sub>x</sub> )O
5a_20c*	4.245(9)	4.245(9)	4.245(9)	90	90	90	76.47(7)	cubic	ferropericlase (Mg <sub>x</sub> ,Fe <sub>1-x</sub> )O

Table 2: Summary of all minerals found in the 23 total diamonds from the São Luiz locality in Juína, Brazil.

Mineral	Number of		
	Inclusions		
ferropericlase (Mgx,Fe <sub>1-x</sub> )O	13		
magnesiowüstite (Mg <sub>1-x</sub> ,Fe <sub>x</sub> )O	14		
wüstite FeO	1		
magnetite (Fe <sub>3</sub> O <sub>4</sub> )	3		
titanomagnetite $Fe_{1+x}(Fe_{2-2x}Ti_x)O_4$	5		
hematite (Fe <sub>2</sub> O <sub>3</sub> )	1		
titanohematite (xFeTiO <sub>3</sub> [1-x]Fe <sub>2</sub> O <sub>3</sub> )	5		
olivine (Mgx,Fe2-x)2SiO4	5		
iron (Fe)	2		
goethite (FeOOH)	1		
ilmenite (FeTiO <sub>3</sub> )	1		
garnet Fe <sub>3</sub> Al <sub>2</sub> (SiO <sub>4</sub> ) <sub>3</sub>	1		
zircon (ZrSiO <sub>4</sub> )	1		

The advantages of high-resolution microtomography extend beyond the X-ray centering procedure as this technique also reveals information on both the number and quality of the inclusions. Super-deep diamonds exhibit rough irregular shapes as well as different surface textures, which often preclude optical observation. Tomography reveals all inclusions even those not visible with optical microscopes as well as provides a way to check that the inclusion is pristine. Super-deep diamonds experience extreme stresses and therefore some exhibit microcracks only visible via tomography (Fig. 3A). These cracks often lead up to or surround an

inclusion, which indicates that an inclusion may have interacted with kimberlitic magma or has cracked as a result of a difference in the elastic relaxation between the inclusion and the host diamond. Such information is lost when inclusions are extracted and yet this information is important when considering how representative an inclusion is of the mantle.

The capability to pre-screen inclusions also exists with microtomography. The reconstructed slices, maps of the absorption, provide the ability to distinguish between high X-ray absorbing inclusions and low X-ray absorbing inclusions. Differences in absorption indicate compositional differences due to the mean atomic weight differences. Inclusions with high iron contents like ferropericlase, (Mg,Fe)O, appear brighter in the tomographic slice than inclusions with lower absorbing material such as silicates or graphite (Fig. 3B; 3C).

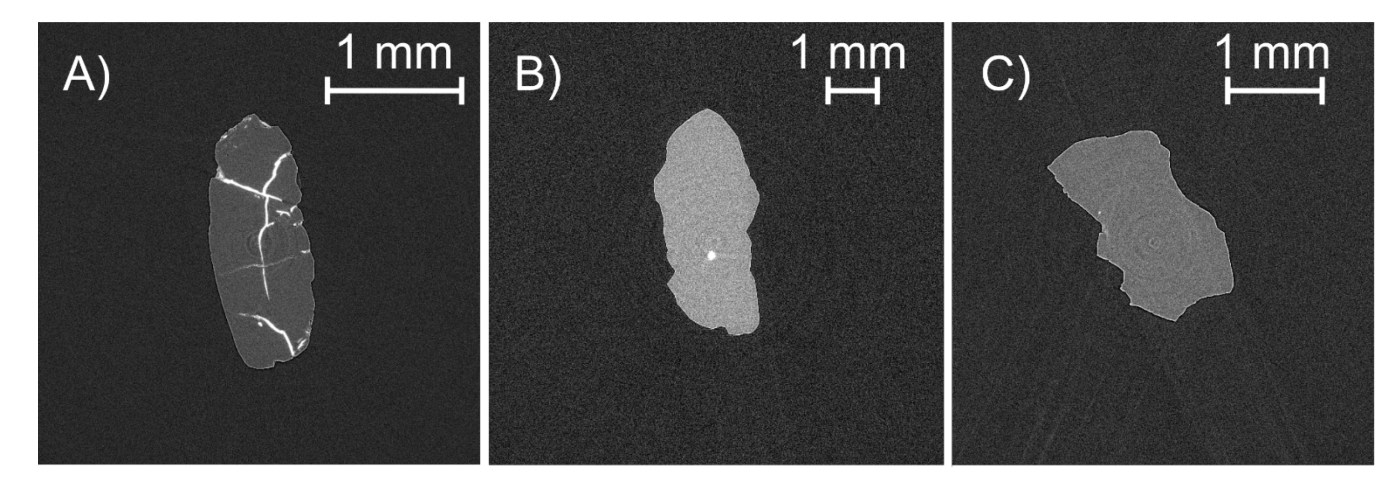


Fig. 3. A) Tomographic slice of diamond 6b\_24 exhibiting multiple cracks. B) Tomographic slice of diamond 6b\_09 with a high absorbing goethite inclusion, FeOOH. C) Tomographic slice of diamond 6b\_56 with a less absorbing silicate inclusion olivine, (Mg,Fe)<sub>2</sub>SiO<sub>4</sub>.

# 4. Conclusion

A fast, high-throughput method developed at GSECARS (Sector 13) of the APS provides the opportunity for dozens of inclusions within a diamond suite to be identified within days (Fig. 4). The high-quality of both the microtomography and X-ray data reveals clues to the inclusion's

history. Identifying all inclusions within a diamond suite garners an insight into the composition and geochemical cycling of Earth's dynamic mantle that remains unattainable with small sample sets. Serving as the only samples from such depths, diamond inclusions hold the key to unlocking the secrets of Earth's mantle.



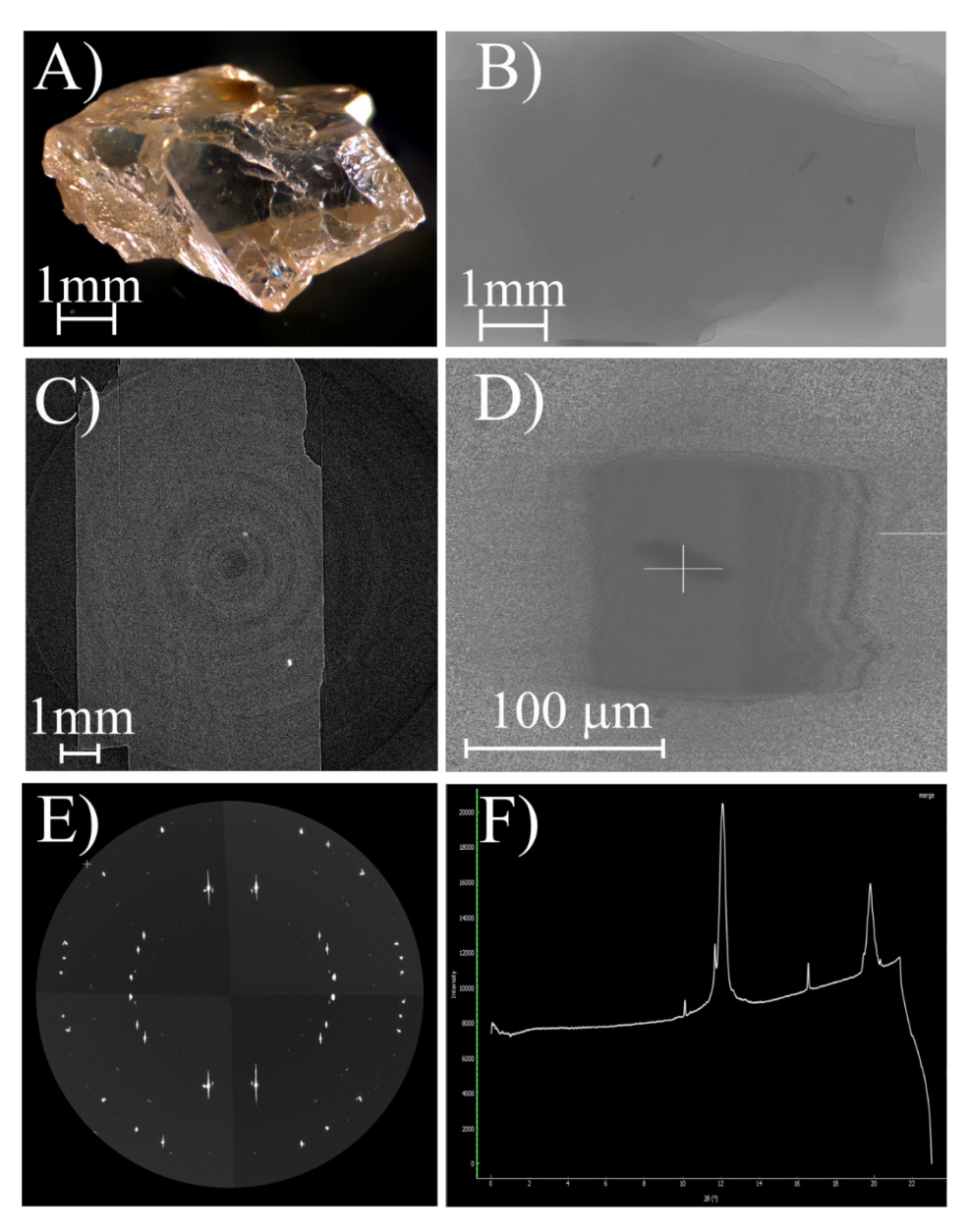


Fig. 4. A) A photomicrograph of Juína diamond 6B\_06. B) Radiograph of diamond 6B\_06 taken at 13-BM-D. C) Reconstructed slice of diamond 6B\_06from 13-BM-D data. Rings seen in image are artifacts. D) Radiograph of one of the ferropericlase inclusions in B taken at 13-BM-C. E)

- Wide scan (180° rotation) XRD image of a ferropericlase inclusion in diamond 6B 06 shown in
- D. F) Integrated Diffraction Pattern of ferropericlase inclusion in diamond 6b 06 image from
- 248 DIOPTAS (Prescher & Prakapenka, 2015).

# **Funding Information**

249

- This study was supported in part through the U.S. National Science Foundation (NSF)
- grant EAR-1853521 to S.D.J. and by the Capital/DOE Alliance Center (CDAC). D.G.P. and
- S.B.S. acknowledge support from the Deep Carbon Observatory (Sloan Foundation). This work
- was performed at GeoSoilEnviroCARS (GSECARS), The University of Chicago, at Sector 13 of
- the Advanced Photon Source (APS), Argonne National Laboratory. GSECARS is supported by
- 255 the NSF through grant EAR-1634415 and U.S. Department of Energy (DOE) grant DE-FG02-
- 256 94ER14466. Experiments at beamline 13-BM-C used the PX^2 facility, supported by
- 257 COMPRES under NSF Cooperative Agreement EAR-1661511. The APS is supported by the
- 258 DOE and operated for the DOE Office of Science by Argonne National Laboratory under
- 259 Contract No. DE-AC02-06CH11357.

References

260

- Angel, R. J., Alvaro, M., Nestola, F., & Mazzucchelli, M. L. (2015). Russian Geology and
- 263 *Geophysics*, **56(1–2)**, 225–234.
- Anzolini, C., Nestola, F., Mazzucchelli, M. L., Alvaro, M., Nimis, P., Gianese, A., Morganti, S.,
- Marone, F., Campione, M., Hutchison, M., & Harris, J. W. (2019). *Geology*, 47, 219-222.
- 266 Bosi, F., Halenius, U., & Skogby, H. (2009). *American Mineralogist*, **94**, 181-189.
- Brown, N. E., Navrotsky, A., Nord, G.L. Jr., & Banerjee, S. K. (1993). American Mineralogist,
- **78**, 941-951.
- Dera, P., Zhuravlev, K., Prakapenka, V., Rivers, M. L., Finkelstein, G. J., Grubor-Urosevic, O.,
- Tschauner, O., Clark, S. & Downs, R. T. (2013). *High Pressure Research*, **33**, 465-484.
- Eng, P. J., Newville, M., Rivers, M. L. & Sutton, S. R. (1998). *The international society for*
- optics and photonics Proceedings, **3449**, 145-156.

- 273 Harte, B. (2011). Science **334**, 51–53.
- Jacobsen, S.D., Reichmann, H.J., Spetzler, H. A., Mackwell, S.J., Smyth, J.R., Angel, R.J., &
- McCammon, C. A. (2002). Journal of Geophysical Research, 107, 1-14.
- Kaminsky, F., Khachatryan, G.K., Andreazza, P., Araujo, D., & Griffin, W. L. (2009). Lithos,
- **112S**, 833-842.
- Kunz, M., Gillet, P., Fiquet, G., Sautter, V., Graafsma, H., Conrad, P., & Harris, J. (2002). Earth
- and Planetary Science Letters, 198, 485–493.
- Nestola, F., Korolev, N., Kopylova, M., Rotiroti, N., Pearson, D.G., Pamato, M.G., Alvaro, M.,
- Peruzzo, L., Gurney, J.J., Moore, A.E., & Davidson, J. (2018). *Nature*, **555**, 237–241.
- Nestola, F., Alvaro, M., Casati, M.N., Wilhelm, H., Kleppe, A.K., Jephcoat, A. P.,
- Domeneghetti, M.C. & Harris, J.W. (2016). *Lithos*, **265**, 334–338.
- Nestola, F., Merli, M., Nimis, P., Parisatto, M., Kopylova, M., Stefano, A. DE., Longo, M.,
- Ziberna, L. & Manghnani, M. (2012). European Journal of Mineralogy, 24, 599–606.
- Nestola, F., Nimis, P., Ziberna, L., Longo, M., Marzoli, A., Harris, J. W., Manghnani, M. H. &
- Fedortchouk, Y. (2011). Earth and Planetary Science Letters, **305**, 249–255.
- Nimis, P., Nestola, F., Schiazza, M., Reali, R., Agrosì, G., Mele, D., Tempesta, G., Howell, D.,
- 289 Hutchison, M.T. & Spiess, R. (2018). *Geology*, **47**, 27-30.
- Palot, M., Jacobsen, S. D., Townsend, J. P., Nestola, F., Marquardt, K., Miyajima, N., Harris, J.
- 291 W., Stachel, T., McCammon, C. A. & Pearson, D. G. (2016). *Lithos*, **265**, 1–7.
- Pearson, D. G., Brenker, F. E., Nestola, F., McNeill, J., Nasdala, L., Hutchison, M. T., Matveev,
- 293 S., Mather, K., Silversmit, G., Schmitz, S., Vekemans, B. & Vincze, L. (2014). *Nature*, **507**,
- 294 221–224.
- 295 Pearson, D. G., Canil, D., & Shirey, S. B. (2003). *Treatise on Geochemistry*, **2**, 171-275.
- 296 Prescher, C. & Prakapenka, V. B. (2015). *High Pressure Research*, **35(3)**, 223–230.
- Prewitt, C. T. & Downs, R. T., *Ultra high-Pressure Mineralogy: Physics and Chemistry of*
- Earth's Deep Interior, edited by R. J. Hemley, 37, 283-317. Washington, D. C.
- 299 Rivers, M. (2018). 16<sup>th</sup> International Conference on Accelerator and Large Experimental
- 300 *Control Systems Proceedings*, 1245-1251.
- 301 Rivers, M. (2010). AIP Conference Proceedings, 1234, 51-54.
- 302 Schneider, C. A., Rasband, W. S. & Eliceiri, K. W. (2012). *Nature Methods*, **9(7)**, 671-675.

- Shirey, S. B., Cartigny, P., Frost, D. J., Keshav, S., Nestola, F., Pearson, G. D., Sobolev, N.V., &Walter M. J. (2013). *Reviews in Mineralogy & Geochemistry*, **75**, 355-421.
- 305 Smith, E.M., Shirey, S.B., Richardson, S. H., Nestola, F., Bullock, E.S., Wang, Jianhua., & Wang W. (2018). *Nature*, **560**, 84-87.
- 307 Stachel, T. & Harris J. W. (2008). *Ore Geology Reviews*, **34(1-2)**, 5-32.
- 308 Stachel, T., Brey, P. & Harris, J. W. (2005). *Elements*, **1(2)**, 73-78.
- Thomson, A.R., Walter, M.J., Kohn, S.C., & Brooker, R. A. (2016). *Nature*, **529**, 76-79.
- 310 Toby, B. H. & Von Dreele, R.B. (2013). *Journal of Applied Crystallography* **46(2)**, 544-549.
- Zhang, D., Dera, P., Eng, P. J., Stubbs, J. E., Zhang, J. S., Prakapenka, V.B. & Rivers, M. L.,
- 312 (2017). *Journal of Visualized Experiments*, **119**, e54660.